Observations of velocities, sand concentrations, and fluxes under velocity-asymmetric oscillatory flows

B. G. Ruessink,[1] H. Michallet,[2] T. Abreu,[3] F. Sancho,[4] D. A. Van der A,[5] J. J. Van der Werf,[6] and P. A. Silva[7]

[1] U-tube measurements of instantaneous velocities, concentrations, and fluxes for a well-sorted, medium-sized sand in oscillatory sheet flow are analyzed. The experiments involved two velocity-asymmetric flows, the same two flows with an opposing current of 0.4 m/s, and a mixed skewed-asymmetric flow, all with a velocity amplitude of 1.2 m/s and flow period of 7 s. We find that the net positive transport rate beneath velocity-asymmetric oscillatory flow results from large, but opposing sand fluxes during the positive and negative flow phase. With an increase in velocity asymmetry and, in particular, velocity skewness, the difference in the magnitude of the fluxes in the two half cycles increases, leading to larger net transport rates. This trend is consistent with the observed increase in skewness of the oscillatory bed shear stress. Phase-lag effects, whereby sand stirred during the negative flow phase has not settled by the time of the negative-to-positive flow reversal and is subsequently transported during the positive flow phase, are notable but of minor importance to the net transport rate compared to earlier experiments with finer sands. In the vertical, the oscillatory flux is positive above the no-flow bed. Within the sheet flow pick-up layer, the oscillatory flux is negative and similar in magnitude to the positive flux induced by the residual flow. The 0.4 m/s opposing current causes more sand to be picked up during the negative than during the positive flow phase. Above the no-flow bed the resulting negative oscillatory flux is comparable in magnitude to the current-related flux.

1. Introduction

[2] As surface gravity waves propagate from deep water onto beaches, they transform in appearance owing primarily to nonlinear wave interactions [*Elgar and Guza*, 1985; *Doering and Bowen*, 1995]. These nonlinear effects amplify the higher harmonics and cause the oscillatory flow beneath the waves to transform from sinusoidal in deep water, through velocity-skewed (preponderance of short, high crests) in the shoaling zone, to velocity-asymmetric (pitched-forward, sawtooth) in the inner surf and swash zone. The local nonlinearity of the near-bed oscillatory flow is important to sand transport. Initially, laboratory and model studies have focused on the predominantly onshore sand transport rates induced by velocity-skewed flows [e.g., *Ribberink and Al-Salem*, 1994; *Davies and Li*, 1997; *O'Donoghue and Wright*, 2004b; *Hassan and Ribberink*, 2005], as velocity-asymmetric flows were assumed to result in zero transport because of their zero velocity skewness [*Roelvink and Stive*, 1989]. Later laboratory studies have shown velocity-asymmetric flows to transport sand in the direction of wave propagation [e.g., *King*, 1991; *Watanabe and Sato*, 2004; *Van der A et al.*, 2009, 2010]. This observation has stimulated the development of practical sand transport formulations [e.g., *Drake and Calantoni*, 2001; *Silva et al.*, 2006; *Nielsen*, 2006; *Gonzalez-Rodriguez and Madsen*, 2007] that include velocity-asymmetry effects; however, the mechanisms leading to nonzero sand transport by velocity-asymmetric waves remain unclear.

[1]Department of Physical Geography, Faculty of Geosciences, Institute for Marine and Atmospheric Research Utrecht, Utrecht University, Utrecht, Netherlands.

[2]Laboratoire des Ecoulements Géophysiques et Industriels, CNRS, Université de Grenoble, Grenoble, France.

[3]Department of Civil Engineering, Polytechnic Institute of Viseu, ESTV, Viseu, Portugal.

[4]LNEC-DHA, National Civil Engineering Laboratory, Lisbon, Portugal.

[5]School of Engineering, King's College, University of Aberdeen, Aberdeen, UK.

[6]Morphology and Sedimentary Systems, Deltares Delft, Netherlands.

[7]CESAM and Departamento de Fisica da Universidade de Aveiro, Aveiro, Portugal.

[3] Based on detailed instantaneous velocity and concentration measurements deep into the sheet flow layer in a fine sand (median grain size d_{50} = 150 μm), *Van der A et al.* [2009] demonstrated that the net sand transport rate beneath velocity-asymmetric flow arises from two complementary effects. First, the time between maximum negative ("offshore") flow and the negative-to-positive flow reversal is small compared to the time needed for the sand to settle. Some of the sand stirred in the negative half cycle will thus persist into and be transported during the positive ("onshore") half cycle. In contrast, maximum positive flow happens early during the positive half cycle and most sand will have settled back to the bed before the positive-to-negative flow reversal. These phase-lag effects between the concentration and the flow velocity thus lead to a positive net transport rate. Secondly, more sand was observed to be picked up during the positive than during the negative flow half cycle because of the positively skewed bed shear stress beneath velocity-asymmetric flow. As suggested by *Nielsen* [1992], the wave boundary layer in the positive, rapidly accelerating half cycle has less time to grow than in the half cycle with less acceleration. This leads to larger (absolute) vertical gradients in flow velocity and, hence, in larger shear stresses [see also *Van der A et al.*, 2008; *Suntoyo et al.*, 2008] and more pick-up of sand in the positive flow half cycle. Numerical simulations with a single-phase, one-dimensional vertical sand transport model [*Ruessink et al.*, 2009] confirm the relevance of both effects, although the importance of phase-lag effects was restricted to situations with a grain size smaller than about 200 μm. Based on the work of *Sleath* [1999], *Foster et al.* [2006] argued that the force on the sand particles due to the shear stress exerted by the flow can be small compared to the force induced by the large free-stream pressure gradient. In that case, the sand is expected to move as a block of several grain diameters high after flow reversal, a phenomenon referred to as plug flow. As for velocity-asymmetric flow this plug flow is restricted to the rapidly accelerating positive half cycle, it results in a net positive transport rate. The free-stream pressure gradient may thus provide the third mechanism for positive net transport rates in velocity-asymmetric oscillatory flow [see also *Drake and Calantoni*, 2001; *Hsu and Hanes*, 2004; *Calantoni and Puleo*, 2006]. In the measurements of *Van der A et al.* [2009], the bed eroded progressively (layer-by-layer) after flow reversal rather than as a block, implying that plug flow was absent.

[4] This paper reports on detailed U-tube measurements of sand concentrations and velocities under sheet flow conditions for full-scale velocity-asymmetric flow. We extend the only previous experiments of this kind [i.e., *Van der A et al.*, 2009] by considering medium sand (d_{50} = 200 μm), mixed skewed-asymmetric flows, and combinations of velocity-asymmetric oscillatory and opposing mean flow. The overall aim of our experiments was to gain better understanding of the mechanisms underlying the positive net transport rates induced by velocity-asymmetric flow and to explore if and how these mechanisms are altered by adding velocity skewness and an opposing mean flow. These additions were motivated by the fact that most natural surf zone waves are mixed skewed-asymmetric [e.g., *Elfrink et al.*, 2006; *Ruessink et al.*, 2009] and are associated with an offshore directed mean current compensating for the onshore

(Stokes) drift above the wave troughs, the undertow. The experimental setup, conditions, and instrumentation are described in section 2. The results on instantaneous velocities, sand concentrations and fluxes are provided in section 3. In section 4 we assess the accuracy of our measurements and discuss the representativeness of our findings to natural conditions. The main conclusions are presented in section 5.

2. Experimental Setup

2.1. Facility

[5] The experiments were conducted in the Large Oscillating Water Tunnel (LOWT) at Deltares, the Netherlands, as part of an European collaborative project. The LOWT, described in detail elsewhere [*Ribberink and Al-Salem*, 1994], is a vertical U-tube with a 14 m long, 0.3 m wide and 1.1 m high horizontal test section, in which full-scale horizontal oscillatory flow can be generated above a 0.3 m thick sand bed. The desired oscillatory flow is imposed by a computer-controlled piston located in one of two vertical cylindrical risers; the other vertical riser is open to the atmosphere. The presence of a recirculating pump system allows a net current to be superimposed on the oscillatory flow.

2.2. Range of Experiments

[6] The experiments involved five oscillatory flows over a well-sorted, medium quartz sand with a median grain size of 200 μm and a geometric standard deviation of 1.2. The piston was controlled to yield regular horizontal free-streamflow u_{∞} of the following general form [*Abreu et al.*, 2010],

$$u_{\infty}(t) = U_w F \frac{\sin(\omega t) + \frac{r \sin \phi}{1 + \sqrt{1 - r^2}}}{1 - r \cos(\omega t + \phi)} + u_t, \quad (1)$$

where t is time, U_w is the velocity amplitude, $\omega = 2\pi/T$ with T the flow period, ϕ is a phase, r is a nonlinearity measure, $F = \sqrt{1 - r^2}$ is a dimensionless factor that ensures the free stream velocity amplitude to equal U_w, and u_t is the net current velocity (the subscript t indicates a time-averaged quantity). *Abreu et al.* [2010] showed that the first term on the right-hand side of equation (1), that is, the oscillatory part of u_{∞}, $\tilde{u}_{\infty}$, is equivalent to $U_w \sum_{k=0}^{\infty} \frac{1}{n^k} \sin[(k+1)\omega t + k\phi]$ with $r = 2n/(1 + n^2)$. For $r = 0$, $\tilde{u}_{\infty}$ is sinusoidal. For $0 < r < 1$, $\tilde{u}_{\infty}$ is asymmetric for $\phi = 0$, skewed for $\phi = -\pi/2$, and mixed asymmetric-skewed for $-\pi/2 < \phi < 0$. For further details, see *Abreu et al.* [2010].

[7] The five flows comprised two asymmetric flows with u_t = 0 m/s (series A), the same two flows superimposed on a net countercurrent u_t = −0.4 m/s (series B), and a mixed asymmetric-skewed flow with u_t = 0 m/s (series C), all with U_w = 1.2 m/s and T = 7 s (Table 1). Table 1 also provides the codes to identify each flow and the dimensionless parameters β_{∞} and R_{∞} to characterize the degree of velocity asymmetry and skewness, respectively. β_{∞} is given by $\tilde{a}_{\infty,\max}^+/(\tilde{a}_{\infty,\max}^+ - \tilde{a}_{\infty,\max}^-)$ [*Watanabe and Sato*, 2004], where $\tilde{a}_{\infty}$ is the free-streamflow acceleration, and $\tilde{a}_{\infty,\max}^+$ and $\tilde{a}_{\infty,\max}^-$ are the maximum positive and negative $\tilde{a}_{\infty}$, respectively. β_{∞} = 0.5 corresponds to sinusoidal and velocity-skewed flows; velocity-asymmetric flows have $\beta > 0.5$. Analogously, $R_{\infty} = \tilde{u}_{\infty,\max}^+/(\tilde{u}_{\infty,\max}^+ - \tilde{u}_{\infty,\max}^-)$ [e.g., *Ribberink*

Table 1. Experimental Conditions[a]

Flow Condition	U_w (m/s)	T (s)	r	ϕ	u_t (m/s)	β_∞	R_∞	As_∞	Sk_∞
A1	1.2	7	0.3	0	0	0.65	0.5	−0.33	0
A3	1.2	7	0.5	0	0	0.75	0.5	−0.59	0
B2	1.2	7	0.3	0	−0.4	0.65	0.5	−0.33	0
B4	1.2	7	0.5	0	−0.4	0.75	0.5	−0.59	0
C1	1.2	7	0.5	$-\pi/4$	0	0.65	0.6	−0.42	0.42

[a]All values are target values; those estimated from the measured free-stream velocity series were marginally different. See Silva et al. (submitted manuscript, 2010) for additional information.

and Al-Salem*, 1994]. R_∞ takes the value of 0.5 for oscillatory flows without velocity asymmetry and above 0.5 for velocity-skewed oscillatory flows. Two alternative measures of velocity asymmetry and skewness, As_∞ and Sk_∞, are also provided in Table 1. The skewness Sk of a time series x is given by $\langle x^3 \rangle / \langle x^2 \rangle^{3/2}$ with the angle brackets denoting a time-average; the asymmetry As is $\langle (\mathcal{H}(x))^3 \rangle / \langle x^2 \rangle^{3/2}$, with $\mathcal{H}(x)$ the Hilbert transform of x. For all five flows, the wave mobility number $\Psi_w = U_w^2 / (\Delta g d_{50})$, where $\Delta = 1.65$ is the relative sand density and $g = 9.81$ m/s^2 is acceleration due to gravity, amounted to 445. This means that the experimental conditions fall well within the sheet flow regime [*Ribberink et al.*, 2008]. Each experiment was conducted for approximately 25 to 30 flow cycles and was repeated several times. This number of cycles ensured that disturbances generated at the boundaries of the tunnel did not propagate into the center section of the LOWT, where all velocity and concentration measurements were obtained.

2.3. Measurements

[8] The complete experimental program involved measurements of (1) net sand transport rates, (2) time-varying velocities, (3) net and time-varying concentrations, and (4) suspended particle size. The net transport rates q_{mc} were computed by numerical integration of the sediment continuity equation using the underwater weight of the sand in the traps below each vertical riser and the bed profiles over the entire width of the LOWT measured before and after each experiment. These bed profiles were determined with the Laser Bed Profiler described by *Van der A et al.* [2010]. The q_{mc} (Table 2), examined in detail by P. A. Silva et al. (Sediment transport in non-linear skewed oscillatory flows: The TRANSKEW experiments, submitted to *Journal of Hydraulic Research*, 2010), show the expected increase with β_∞ [*Watanabe and Sato*, 2004; *Van der A et al.*, 2010] and R_∞ [*Dibajnia and Watanabe*, 1998; *Ruessink et al.*, 2009]. In the following subsections, we focus on the time-varying velocity and concentration measurements in the sheet flow and suspension layer.

2.3.1. Velocities

[9] Two methods were used to measure time-varying velocities. An Electromagnetic Current Meter (EMCM) was deployed at 300 mm above the bed to measure the free-stream velocity. Its sampling rate was 100 Hz. Detailed velocity measurements from approximately 150 mm above the bed to within the sheet flow layer were conducted with an Acoustic Doppler Velocimeter Profiler (ADVP) [*Hurther and Lemmin*, 2001]. The ADVP is composed of a sensor emitting at 2 MHz and two receivers positioned at about

350 mm above the sand bed and 79 mm to the center of the emitter. The acoustic pulse is repeated at 1.6 kHz. The phase shift of the backscattered signal on the two receivers is recorded every 4 μs. The ADVP data were processed into instantaneous (50 Hz) vertical profiles of horizontal (along the LOWT) u and vertical w velocities. The vertical resolution of the u and w profiles is 3 mm. From the available flow cycles we computed phase-averaged oscillatory and turbulent velocity quantities. To suppress noise related to the limited number of available cycles, we subsequently downsampled both the oscillatory and turbulent velocities to 10 Hz by averaging over five consecutive velocity estimates. Also, the small (a few millimeters at most) bed level changes during each experiment were accounted for in the ADVP postprocessing. In the following, the vertical coordinate is denoted z and is positive upward, with $z = 0$ the level of the initial no-flow bed.

[10] For the three conditions without a net counter current (A1, A3, and C1), suspended sand levels at $z > 30$ mm were insufficient to obtain reliable ADVP measurements during parts of the flow cycle, especially around the reversal from negative to positive flow. This resulted in unrealistically high turbulence quantities and in oscillatory velocity estimates closer to 0 m/s than observed in the EMCM series. The ADVP also produces velocity estimates within the sheet flow layer below the no-flow bed ($z = 0$). H. Michallet et al. (Sheet flow layer dynamics under skewed oscillatory flows, manuscript in preparation, 2011) found reasonable agreement between these u estimates and sand particle velocities estimated from two Conductivity Concentration Meter (CCM) probes (see *Abreu et al.* [2009] for details) deployed concurrently with the ADVP (see section 2.3.2). This suggests that the ADVP velocity estimates below the no-flow bed level are realistic.

2.3.2. Concentrations

[11] Three methods were used to measure sand concentrations c. Time-averaged concentrations, c_t, were measured using ten transverse suction samplers (TSS) [*Bosman et al.*, 1987], typically for the $z = [25–250]$ mm range. From each obtained sample, the median grain size was determined with a sediment settling tube. Vertical profiles of time-varying concentrations, $c(z,t)$, down to 5 mm above the no-flow bed were obtained with an Acoustic Backscatter Sensor (ABS) [*Thorne and Hanes*, 2002]. The ABS, mounted in one of the top lids of the LOWT, operated at 1.0, 2.0 and 4.0 MHz and collected backscatter profiles at 80 Hz with a 5 mm bin size. The available 80 Hz backscatter profiles were root-mean-square downsampled to 10 Hz and then phase-averaged. During each experiment, the bed change at the ABS location was always less than one bin. The conversion from backscatter to concentration requires knowledge of the system constants of the ABS [*Betteridge et al.*,

Table 2. Net Sand Transport Rates

Flow Condition	q_{mc} (kg/m/s)	q^+ (kg/m/s)	q^- (kg/m/s)	q (kg/m/s)
A1	0.054	0.884	−0.786	0.098
A3	0.114	0.645	−0.500	0.145
B2	−0.378	0.262	−0.889	−0.627
B4	−0.221	0.399	−0.851	−0.452
C1	0.185	0.547	−0.309	0.238

2008], one for each of the three transducers. We used the explicit calibration procedure outlined by *Thorne and Hanes* [2002], using the TSS sample obtained nearest to the bed for flow A3. The median grain size of the suspended sand for this flow was independent of z (~174 μm), an important assumption underlying the explicit calibration approach [*Thorne and Hanes*, 2002]. Using TSS data from other flows did not change the system constants noteworthy [*Ruessink*, 2009]. With the system constants now known from the explicit calibration, we used the implicit approach of *Thorne and Hardcastle* [1997] to convert the phase-averaged backscatter to concentration profiles.

[12] The ABS yields 3 concentration profiles (one for each transducer) at each time step. We found the three profiles to be essentially identical in the range between 10 to $\approx$ 40 mm above the bed. In the lowest bin (5 mm above the bed), the 4 MHz concentration estimates were often substantially larger than those of the 1 and 2 MHz signals, presumably because of saturation of the 4 MHz signal [e.g., *Thorne et al.*, 1995]. Above $\approx$ 40 mm, the three concentration estimates also deviated, but, as we will see below, the concentrations here are small ($<\mathcal{O}(10^{-2})$ kg/m^3), presumably close to the ABS noise level [*Ruessink*, 2009]. To arrive at a single concentration profile, we computed the standard deviation and the mean of the three estimates at each height. When the ratio of the standard deviation to the mean was less than 0.2, the concentration was taken as the mean of the three estimates. When the ratio exceeded 0.2, the outlier was discarded and the concentration was taken as the mean of the remaining two estimates. The 0.2 threshold was obtained with trial and error and was found to be sufficiently accurate to remove the aforementioned unrealistically high, near-bed concentrations estimated from the 4 MHz transducer. This averaging scheme was applied separately to each time step within the flow cycle. For further details, see *Ruessink* [2009].

[13] Concentrations in the sheet flow layer were measured using two Conductivity Concentration Meter (CCM) [*Ribberink and Al-Salem*, 1995; *McLean et al.*, 2001] probes, installed into the tunnel from below, through the tunnel bottom. The measuring principle is based on the conductivity change of a sand-water mixture due to the variation of the quantity of nonconductive sand present in the measurement volume. The concentration range that can be measured is about 100–1600 kg/m^3 [*Ribberink and Al-Salem*, 1995]. Because vertical concentration gradients in the sheet flow layer are high and the bed level gradually changed by several millimeters during each experiment, the CCM concentration series had to be carefully postprocessed [*Abreu et al.*, 2009] to yield accurate concentration data at specific heights with respect to the no-flow bed. The postprocessing was aided by concurrent video observations of a ruler attached to the glass wall of the LOWT near the CCM probes. From the video, the bed level at the tunnel sidewall was determined regularly. This, in combination with the reading from the CCM's positioning gauge and the assumption that the bed was horizontal across the tunnel, resulted in elevation estimates of the CCM for each flow cycle. All available CCM flow cycles for a specific flow were subsequently grouped in bins between -7 to 3 mm with respect to the no-flow bed, with a 1 mm resolution and a 0.4 mm bin height. All cycles with an estimated height not

belonging to a specific bin were discarded [*Abreu et al.*, 2009]. Similar to the ABS data, the CCM data were phase-averaged with a 10 Hz resolution. Ensemble-averaged series with concentration estimates less than 100 kg/m^3 during part of the flow cycle were considered inaccurate and, therefore, were discarded as well. From the phase-averaged CCM series, we determined the erosion depth, $\delta_e(t)$, as the height with respect to the no-flow bed level where the instantaneous concentration equals the undisturbed bed concentration c_0. Values of c_0 differed slightly between the five flows, varying from about 1400 to 1550 kg/m^3. Similar c_0 values were reported by *Dohmen-Janssen et al.* [2002, Figure 14] and *Hassan and Ribberink* [2005, Figure 7].

3. Results

3.1. Velocities

[14] The first column in Figure 1 shows the ADVP-measured phase-averaged oscillatory velocities $\tilde{u}$ of A1, C1 and B2 for $z \geq 0$ as a function of dimensionless time t/T. The results for A3 are comparable to those of A1 and are therefore not shown separately. The same goes for B2 and B4. The plots show various well-known features of oscillatory boundary layer flow: the velocity decays toward 0 as the bed is approached; near the bed, the velocity turns before the free stream velocity; and, the velocity is largest in the range $z = 10$–30 mm. The vertical structure of the phase lead ψ between each $\tilde{u}$ series and the free stream velocity was determined from cross-spectral analysis; the ψ values in the second column of Figure 1 are those for the fundamental harmonic $f = 1/T \approx 0.143$ Hz. For all five flows, ψ increases from 0 at $z > 30$ mm and peaks at approximately 15° at $z = 6$ mm. Below $z = 6$ mm, ψ reduces to less than 10° for A1, A3 and C1, and even to about 0° for B2 and B4 at $z = 0$ (Figure 1, second column). A similar vertical ψ structure has been observed in other mobile-bed experiments [*McLean et al.*, 2001; *Malarkey et al.*, 2009] and in two-phase model simulations [*Dong and Zhang*, 2002; *Malarkey et al.*, 2009], but contrasts markedly with the further increase in ψ at $z = 0$ in the velocity-asymmetric, fixed-bed experiments of *Van der A et al.* [2008]. The contrasting behavior may point to an effect of the high near-bed sand concentrations on the flow in the wave boundary layer [*Malarkey et al.*, 2009]. Interestingly, the stronger reduction in ψ for the experiments with a nonzero mean flow is also apparent from *McLean et al.*'s [2001] data, suggesting that this stronger reduction is a mean-flow effect.

[15] The velocity overshoot is explored in the third column of Figure 1, which shows the ratios $\tilde{u}_{max}^+/\tilde{u}_{\infty,max}^+$ and $\tilde{u}_{max}^-/\tilde{u}_{\infty,max}^-$ at each z. For the four velocity-asymmetric flows (A1, A3, B2, and B4), the maximum positive overshoot is reached at slightly lower heights and its magnitude is slightly higher than that of the maximum negative overshoot. For A1, for instance, the positive (negative) overshoot is maximum at $z \approx$ 24 (39) mm, with $\tilde{u}_{max}^+/\tilde{u}_{\infty,max}^+ \approx 1.09$ and $\tilde{u}_{max}^-/\tilde{u}_{\infty,max}^- \approx 1.07$. With an increase in velocity asymmetry, the maximum positive overshoot is reached at lower z and increases in magnitude. For C1, in which the free-stream velocity is also skewed, the heights of maximum positive and negative overshoot are about the same; they are also of about equal magnitude, $\tilde{u}_{max}^+/\tilde{u}_{\infty,max}^+$ and $\tilde{u}_{max}^-/\tilde{u}_{\infty,max}^-$ are both ≈ 1.07.
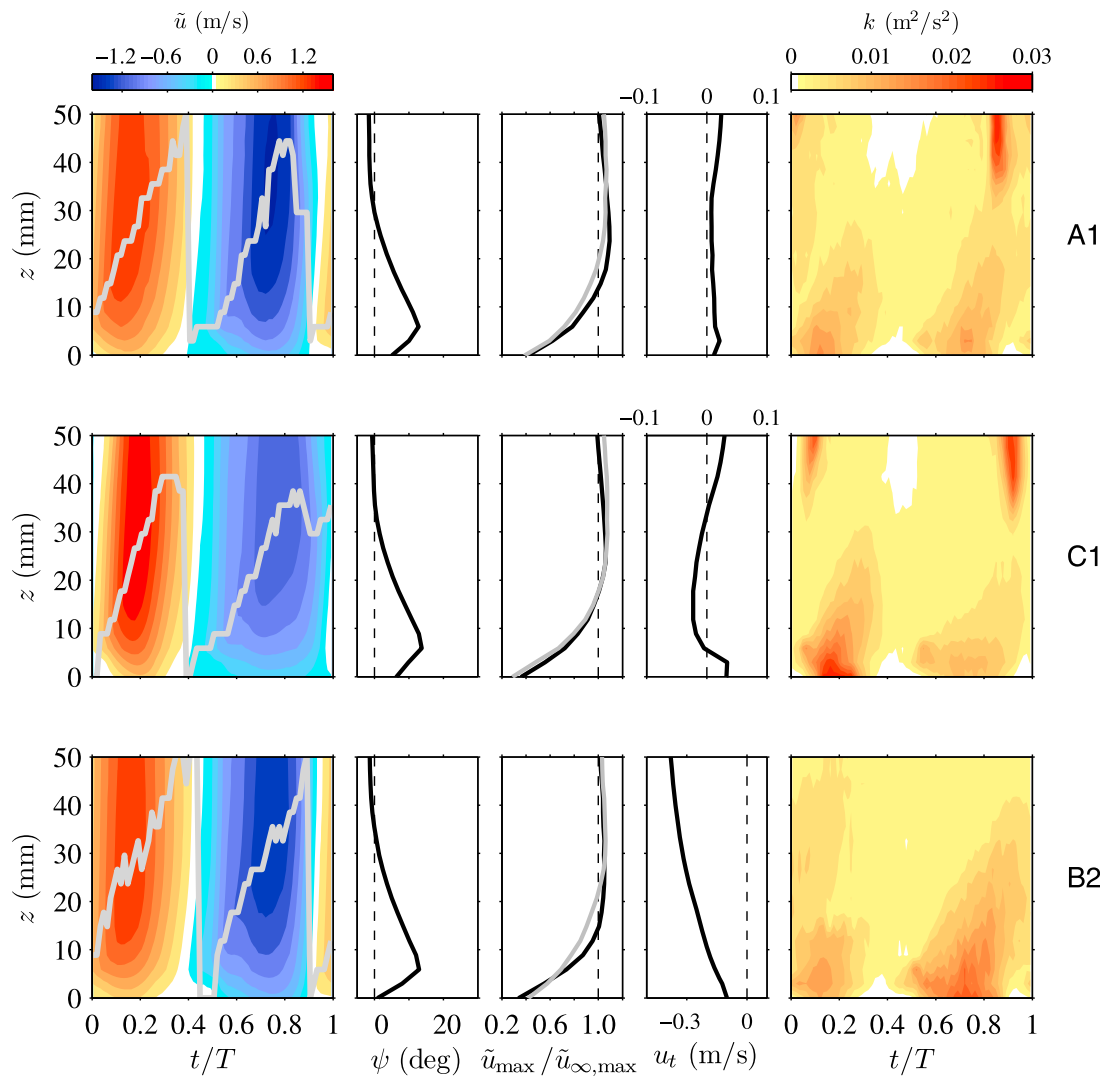
Figure 1. Velocity data at (from top to bottom) A1, C1, and B2. (first column) Time-space diagram of oscillatory velocity $\tilde{u}$; the gray line shows the estimated location of the top of the wave bottom boundary layer. (second column) Vertical structure of the phase lead ψ of $\tilde{u}$ over $\tilde{u}_\infty$. (third column) Vertical structure of (black) normalized maximum positive and (gray) maximum negative oscillatory velocity, $\tilde{u}^+_{\max}/\tilde{u}^+_{\infty,\max}$ and $\tilde{u}^-_{\max}/\tilde{u}_{\infty,\max}$. (fourth column) Vertical structure of mean flow u_t. (fifth column) Time-space diagram of turbulent kinetic energy k, estimated as [*Svendsen*, 1987] $k = 1.33 \times 0.5(u'^2 + w'^2)$, where u' and w' are the phase-averaged horizontal and vertical turbulence velocities, respectively. The nonzero u_t for A1 and C1 is the residual flow; no opposing or following current was imposed for these two conditions; see Table 1. The suspended sand levels were insufficient to obtain reliable ADVP measurements at $z > 30$ mm for A1 and C1; this explains the unrealistically large k at these levels for both conditions.

[16] The vertical structure of the time-averaged residual flow, $u_t(z)$, for A1 (Figure 1, fourth column) and A3 is rather featureless, except for $z < \approx 6$ mm where the positive residual flow (or, streaming) is larger than elsewhere in the vertical. The C1 $u_t(z)$ resembles the structure measured previously for velocity-skewed oscillatory flow [*Ribberink et al.*, 2008, Figure 7]. The difference in A1 and C1 $u_t(z)$ is mostly likely due to the different degrees of turbulence asymmetry during successive oscillatory flow half-cycles [e.g., *Ruessink et al.*, 2009]. For A1 the turbulence kinetic energy k beneath the positive and negative flow cycle are comparable, while those for C1 are clearly asymmetric, with higher k beneath the positive flow cycle (Figure 1, fifth column). The turbulence asymmetry for C1 causes the negative residual flow for $z \approx 6$–30 mm and the positive residual flow higher up in the vertical [*Davies and Li*, 1997]. The positive streaming nearer to the bed ($z < 6$ mm) can be explained by the fact that, due to velocity skewness, the lowest levels in the sheet flow layer mobilized by the peak positive velocities are not mobilized during negative flow [*Ribberink et al.*, 2008]. The negative, asymmetry-induced streaming is therefore unable to penetrate fully into the sheet flow layer, which results in a slight positive streaming (≈ 0.03 m/s) within the sheet flow layer. The positive u_t for A1 and A3 very close to the bed contrasts with the negative near-bed u_t observations of *Van der A et al.* [2008] obtained
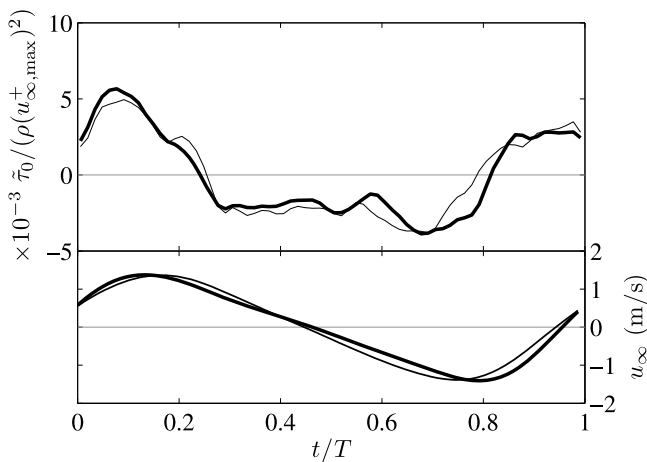
Figure 2. Time series of the oscillatory bed-shear-stress $\tilde{\tau}_0$, normalized by $\rho\,(\tilde{u}_{\infty,\max}^+)^2$, for (solid line) A1 and (thick solid line) A3, estimated using equation (2) and $z_\infty = 30$ mm. The bottom panel shows the free-stream velocity u_∞ for reference.

above a fixed bed, supporting further *Ribberink et al.*'s [2008] suggestion that the near-bed positive streaming is a mobile-bed effect. Interestingly, the A1 and A3 u_t are positive in the entire vertical. In U-tube flows, friction on the sidewalls induces small three-dimensional secondary flows. Whether the positive u_t are related to these spurious currents cannot be determined from our data. This would require a complete three-dimensional mapping of the flow with a nonintrusive instrument, but this has not been performed so far.

[17] For A1, A3 and C1, the maxima in k at $z = 0$ are in phase with maximum positive and negative free-stream velocity. The k maxima propagate up from the bed to lag those at $z = 0$ by about 0.7–0.8 s at $z = 20$ mm. This corresponds to an upward propagation velocity of maximum k of about 0.027 m/s. For B2 and B4, the maximum in k at $z = 0$ under maximum negative flow clearly exceeds the maximum under maximum positive flow and propagates up to higher levels (Figure 1, fifth column). Moreover, the turbulence generated under maximum negative flow can still be seen at $z > 20$ mm after reversal to positive flow, causing $k(z)$ around maximum positive flow ($t/T \approx 0.1$) to be double-peaked at $z = 0$ and ≈ 30 mm.

[18] Also shown in Figure 1 (first column) is the instantaneous thickness of the wave bottom boundary layer, δ_w. Here, δ_w at each t/T is taken as the distance between $z = 0$ and the height where $\tilde{u}(z)$ is maximum and has the same sign as $\tilde{u}(0)$. The boundary layer can be seen to build up approximately linearly after flow reversal to reach a maximum thickness of about 30 to 50 mm just before the next flow reversal. For the asymmetric flows without a countercurrent (A1 and A3), δ_w under maximum positive flow is smaller than under maximum negative flow because the wave bottom boundary layer has less time to grow. This difference in thickness increases with velocity asymmetry and has been suggested to be one of the main causes of positive net transport under asymmetric flows [*Nielsen*, 1992, 2006; *Suntoyo et al.*, 2008; *Van der A et al.*, 2008];

the (absolute) velocity gradients and, as a consequence, the bed shear stresses, in the rapidly accelerating half cycle are higher than in the half cycle with less acceleration. To examine the resulting positive skewness in bed shear stress under asymmetric flows, we estimated time series of the oscillatory bed shear stress $\tilde{\tau}_0(t)$ for A1 and A3 using [e.g., *Dick and Sleath*, 1992]

$$\tilde{\tau}_0(t) = \int_0^{z_\infty} \frac{\partial(\rho \tilde{u}_\infty(t) - \rho_m(z)\tilde{u}(z,t))}{\partial t}\, dz, \qquad (2)$$

where z_∞ is a height above the boundary layer and $\rho = 1000$ kg/m^3 is water density. The density of the fluid-sediment mixture ρ_m was estimated as $\rho_m(z) = (1 - c_t(z)/\rho_s)\rho + c_t(z)$, where $\rho_s = 2650$ kg/m^3 is sand density and $c_t(z)$ is the vertical profile of time-averaged sand concentrations. As $\tilde{u}$ may not be accurate around flow reversal when $z > 30$ mm, we take $z_\infty = 30$ mm in equation (2). Although ideally z_∞ should have been higher, using an even lower z_∞ of 21 mm resulted in about identical $\tilde{\tau}_0(t)$ (not shown). The obtained $\tilde{\tau}_0$ series (Figure 2) indeed have higher values under positive than under negative flow, and are positively skewed, with an increase in skewness with an increase in velocity asymmetry ($Sk_{\tilde{\tau}0}$ for A1 and A3 were 0.27 and 0.48, respectively). The use of a time-dependent $\rho_m(z,t) = (1 - c(z,t)/\rho_s)\rho + c(z,t)$ in equation (2) instead of $\rho_m(z)$ had negligible effects on $\tau_0(t)$ and its skewness for both A1 and A3. For C1 (not shown), $Sk_{\tilde{\tau}0}$ was 0.57.

3.2. Concentrations

[19] Figure 3 presents the time-dependent and time-averaged concentrations as a function of z for A1, C1, and B2; again, results for A3 and B4 are not shown. It is reassuring that the c_t profiles based on the ABS data connect well to those of the CCM and that below $z \approx 30$ mm, the TSS-based c_t agree well with those of the ABS. The latter was invoked for A3 because of the explicit ABS calibration; the good agreement for the other four flows indicates that the A3-based system constants are applicable to these four flows as well. Higher up in the vertical, the ABS c_t are persistently lower than the TSS c_t, with the difference increasing to almost an order of magnitude ($\mathcal{O}(0.1)$ versus $\mathcal{O}(1)$ kg/m^3 for the flows without a countercurrent) at $z \approx 50$ mm. Possibly, the intrusion of the TSS into the flow produces more turbulence and mixing locally, biasing the concentration levels at $z > \approx 30$ mm. Also, size sorting is not accounted for in the conversion of ABS voltage to concentration estimates and this may lead to errors in the ABS-based concentration estimates. Although the reasons for the difference in the ABS and TSS c_t are not entirely clear, the effect of this difference on the vertical distribution of the sand fluxes will be minimal as both the ABS and TSS c_t are low compared to c_t at $z < \approx 30$ mm. Each panel with the time-dependent concentration also shows the instantaneous erosion depth δ_e, determined as the c_0 contour, and the instantaneous top of the sheet flow layer, δ_s. The latter was determined as the contour of $0.125c_0$; as pointed out by *Dohmen-Janssen and Hanes* [2002], the motivation for this choice is that at lower concentrations (i.e., in the suspension layer) intergranular stresses are negligible and the concentration profile is determined by turbulent diffusion processes.
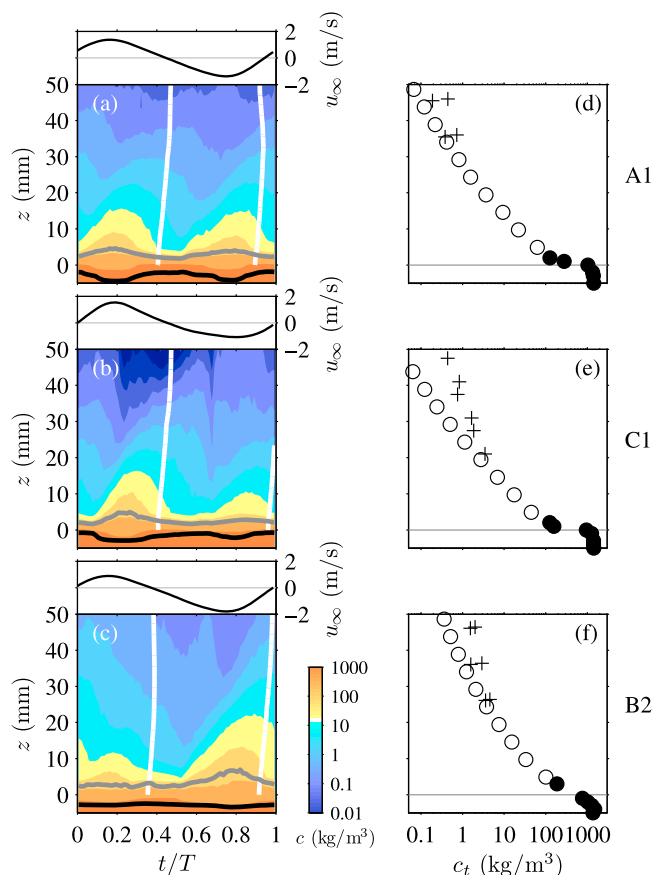
Figure 3. Concentration data at (from top to bottom) A1, C1, and B2. (first column) Time-space diagram of instantaneous concentration c. The curved black and gray lines are the instantaneous erosion depth δ_e and the top of the sheet flow layer δ_s, respectively. The approximately vertical white lines are the moments of flow reversal. Above each diagram, the free-stream velocity u_∞ is given for reference. (second column) Time-averaged concentration profiles $c_t(z)$. Observations from the CCM, ABS, and TSS are indicated by the filled circles, open circles, and pluses, respectively. In each $c_t(z)$ panel, the horizontal gray line is the no-flow bed position, $z = 0$.

[20] The instantaneous concentration data within the sheet flow layer show the expected [e.g., *O'Donoghue and Wright*, 2004a; *Hassan and Ribberink*, 2005; *Van der A et al.*, 2009] difference in behavior above and below $z \approx 0$ mm for all five flows. Below $z = 0$ mm, concentrations are high ($c_t > \sim 750$ kg/m^3) and vary in antiphase with u_∞. The $\delta_e \leq z \leq 0$ range thus represents the pick-up layer. As u_∞ increases, sand is picked up and entrained in the upper sheet flow layer ($0 < z \leq \delta_s$) and the suspension layer ($z > \delta_s$); as a consequence, c reduces and δ_e increases. Concentrations in the pick-up layer increase again as u_∞ decreases and sand settles back to the bed. This results in a reduction in δ_e, but δ_e is never zero, even at times of flow reversal. The temporal evolution of δ_e thus indicates progressive erosion and sedimentation in response to the time variation of the bed shear stress. We find no indications that after flow reversal the sand starts to move as a block of several grain

diameters deep, as expected when the forces on the sand particles are dominated by the free-stream pressure gradient. In the upper sheet flow the concentrations vary approximately in phase with u_∞, while within the suspension layer the concentration increasingly lags that in the upper sheet flow layer. For A1, for example, the concentration at $z = 15$ (25) mm lags that at $z = 5$ mm by approximately 0.4 (1.0) s.

[21] The character of the concentration peaks and the temporal evolution of the sheet flow layer thickness $\delta_{SF} = \delta_s + |\delta_e|$ (Figure 4) differ substantially between the flows without and with velocity skewness (A1, A3 versus C1) and those without and with a countercurrent (A1, A3 versus B2, B4). For A1, the concentration peaks during the positive and negative flow phase (hereafter denoted u_∞^+ and u_∞^-, respectively) are very similar in magnitude and temporal evolution (Figure 3a), and the maximum δ_{SF} during u_∞^+ (~ 8 mm) is only marginally larger ($\sim 10\%$) than during u_∞^- (Figure 4a). For A3, the δ_{SF} during the negative-to-positive flow reversal ($t/T \sim 0.95$) is about 1.5 mm larger than during the other reversal ($t/T \sim 0.45$). With the increase in velocity asymmetry from A1 to A3, the time difference between $u_{\infty,\text{max}}^-$ and the negative-to-positive flow reversal has reduced by 0.7 s. Accordingly, the sand stirred in the negative flow phase has less time to settle back to the bed, resulting in the persistence of some sand into the positive flow phase. Thus, the larger difference in δ_{SF} between the two flow reversals points to the increasing importance of phase lag effects to sand transport rates beneath more asymmetric flow. Compared to the $d_{50} = 150\ \mu$m results of *Van der A et al.* [2009], the importance of phase-lag effects to the transport rate for the present $d_{50} = 200 \mu$m sand appears rather limited. For the mixed velocity skewed-asymmetric flow (C1), the sand is entrained higher into the suspension layer during u_∞^+ than u_∞^- (Figure 3b); these differences are consistent with the differences in maximum erosion depth below both flow phases (Figure 3b) and cause the maximum δ_{SF} during u_∞^- to be approximately 60% of that during u_∞^+ (Figure 4a). In the B2 and B4 tests, the concentration peak during u_∞^- is considerably larger in magnitude than during u_∞^+ (Figures 3c), as expected from the large $u_{\infty,\text{max}}^-$ and consistent with our earlier observations for the turbulent kinetic energy (Figure 1, fifth column). Compared to the flows without the countercurrent, the sand also reaches further into the suspension layer, causing the B2 and B4 c_t profiles to be steeper than those of A1, A3, and C1, compare Figure 3f to Figures 3d–3e. The temporal variation in the B2 and B4 δ_e is small compared to that in the other three flows, compare Figure 3c to Figures 3a–3b. Thus, the temporal variation in the B2 and B4 δ_{SF} in Figure 4b is due primarily to that in the top of the sheet flow layer. As can be seen in Figure 4b, the increase in velocity asymmetry from B2 to B4 leads to an increase in δ_{SF} at u_∞^+ and a decrease in δ_{SF} at u_∞^-. While the difference between both δ_{SF} is about 3.5 mm for B2, it reduced to less than 2 mm for B4.

3.3. Sand Fluxes

[22] The instantaneous horizontal sand flux is the product of the instantaneous flow velocity and sand concentration, $\phi(z,t) = u(z,t)\ c(z,t)$. Our measurements for $u(z,t)$ and $c(z,t)$ were neither of the same volume nor collocated. To obtain $\phi(z,t)$ estimates, the ADVP data were interpolated to each z level for which a concentration time series was available;
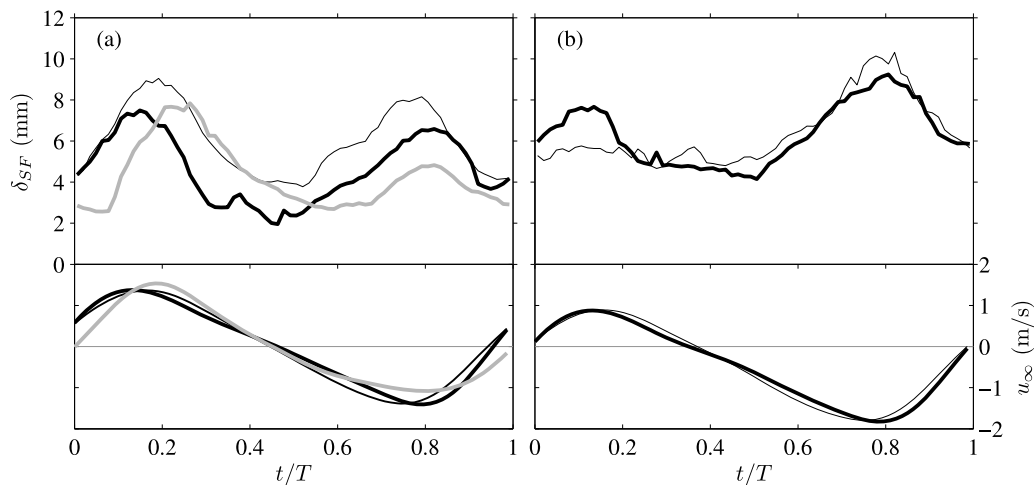
Figure 4. Time series of the thickness of the sheet flow layer, δ_{SF}, for (a) A1 (solid line), A3 (thick solid line), and C1 (thick gray line) and for (b) B2 (solid line) and B4 (thick solid line). The bottom panels show the free-stream velocity u_∞ for reference.

in the pick-up layer, we assumed a linear velocity profile between $u = 0$ at δ_e and the ADVP velocity estimate at $z = 0$ when $-3 < \delta_e < 0$ mm or at $z = -3$ mm when $\delta_e < -3$ mm. Because the concentrations in the pick-up layer are large, even small uncertainties in u may profoundly affect the sand fluxes. We return to the uncertainty in the sand-flux estimates in section 4.1. Because the flow in a U-tube is horizontally uniform, the along-tube separation of the $u(z,t)$ and $c(z,t)$ measurements does not impact our flux estimates.

[23] As can be seen in the $\phi(z,t)$ diagrams in Figures 5a–5c, the flux is highest in the sheet flow layer, at $z \approx 0$, for all flows. The largest magnitudes are reached for the two flows (A1 and A3) without velocity skewness and without a net counter current. For A1, for example, $\phi(z,t)$ reaches about 405 kg/m^2/s and -390 kg/m^2/s at $z = 0$ under $\tilde{u}^+_{\infty,\text{max}}$ and $\tilde{u}^-_{\infty,\text{max}}$, respectively. For B4, these numbers are a mere 205 and -285 kg/m^2/s. In general, the fluxes in the sheet flow layer vary in phase with the free stream velocity. Relatively high fluxes are also found immediately after reversal from negative to positive flow for all cases without velocity skewness. In contrast, similarly high fluxes are absent after the other flow reversal. The high sand fluxes after reversal from $\tilde{u}^-_\infty$ to $\tilde{u}^+_\infty$ result from the aforementioned phase-lag effects.

[24] The time-averaged fluxes, $\phi_t(z) = 1/T \int_0^T \phi(z,t)\mathrm{d}t$, for A1 and A3 are positive throughout the entire vertical (Figure 5d for A1). The values are very small compared to the maximum instantaneous fluxes because the very large fluxes below $\tilde{u}^+_\infty$ and $\tilde{u}^-_\infty$ almost cancel each other out. For A1, for example, the $\phi_t(0) \approx 4.5$ kg/m^2/s is 1% only of the maximum instantaneous flux. Also shown in Figure 5d are the time-averaged oscillatory and current-related fluxes, $\tilde{\phi}_t(z)$ and $\overline{\phi}_t(z)$, calculated as $\tilde{\phi}_t(z) = 1/T \int_0^T \tilde{u}(z,t)\tilde{c}(z,t)\mathrm{d}t$ and $\overline{\phi}_t(z) = \overline{u}_t(z)\overline{c}_t(z)$, respectively. Both $\tilde{\phi}_t(z)$ and $\overline{\phi}_t(z)$ show an intriguing vertical structure. For $z > 0$ mm $\tilde{\phi}_t(z)$ is positive and dominates over the virtually negligible flux contribution by the residual flow. This pattern changes completely within the pick-up layer; here, $\tilde{\phi}_t(z)$ is negative and slightly less in magnitude than the positive $\overline{\phi}_t(z)$. At first glance, the negative $\tilde{\phi}_t(z)$ may be counterintuitive; however, in the pick-up

layer, concentrations decrease with increasing free-stream velocity and for a given z, they do so more under the positive than under the negative half cycle. The negative $\tilde{\phi}_t(z)$ is thus due to lower (higher) concentrations during u^+_∞ (u^-_∞). Although the mean velocities within the pick-up layer are estimated to be less than 1 cm/s, the high mean concentrations ($>\approx700$ kg/m^3) cause $\overline{\phi}_t$ to exceed $\tilde{\phi}_t$, and ϕ_t to remain positive. Figure 5d thus indicates that the positive time-averaged and depth-integrated transport rate $q = \int_{z\text{min}}^{z\infty} \phi_t(z)$ dz (z_{min} is a z in the undisturbed bed) is due primarily to positive oscillatory flux above the no-flow bed and positive flux induced by the residual flow in the pick-up layer. The same pattern arises for the mixed skewed-asymmetric case (C1); see Figure 5e.

[25] The oscillatory flux for the two flows with a countercurrent is negative (Figure 5f for B2), thus, against the direction of wave propagation for $z > 0$. This results from the higher concentrations during the negative than during the positive flow phase (Figure 3c). Intriguingly, the oscillatory and current-related flux are of approximately equal magnitude (Figure 5f). In other words, the countercurrent does not induce a negative net flux because of the negative current-related flux alone; the oscillatory flux also becomes negative and adds considerably to the net negative flux above the pick-up layer. As observed for the three flows without a net current, the oscillatory flux changes sign around $z = 0$ and is thus positive within the pick-up layer; the current-related flux remains negative and now dominates over the oscillatory flux.

[26] As demonstrated in Figures 5g–5i, the time-dependent, depth-integrated fluxes, $\phi_d(t) = \int_{z\text{min}}^{z\infty} \phi(z,t)\mathrm{d}z$, vary approximately in phase with the free-stream velocity. From Figures 5g–5h it can also be deduced that q is a close balance between the net flux during the positive and negative flow phase, $q^+ = \int_{z\text{min}}^{z\infty} \phi^+_t$ dz and $q^- = \int_{z\text{min}}^{z\infty} \phi^-_t \mathrm{d}z$, respectively, for A1 and C1. This is quantified for all 5 flows in Table 2. Table 2 further highlights that q increases with velocity asymmetry and skewness, consistent with the observed increase in $Sk_{\tilde{\tau}0}$. Interestingly, the increase in q is primarily due to a marked reduction in q^-. For the increase
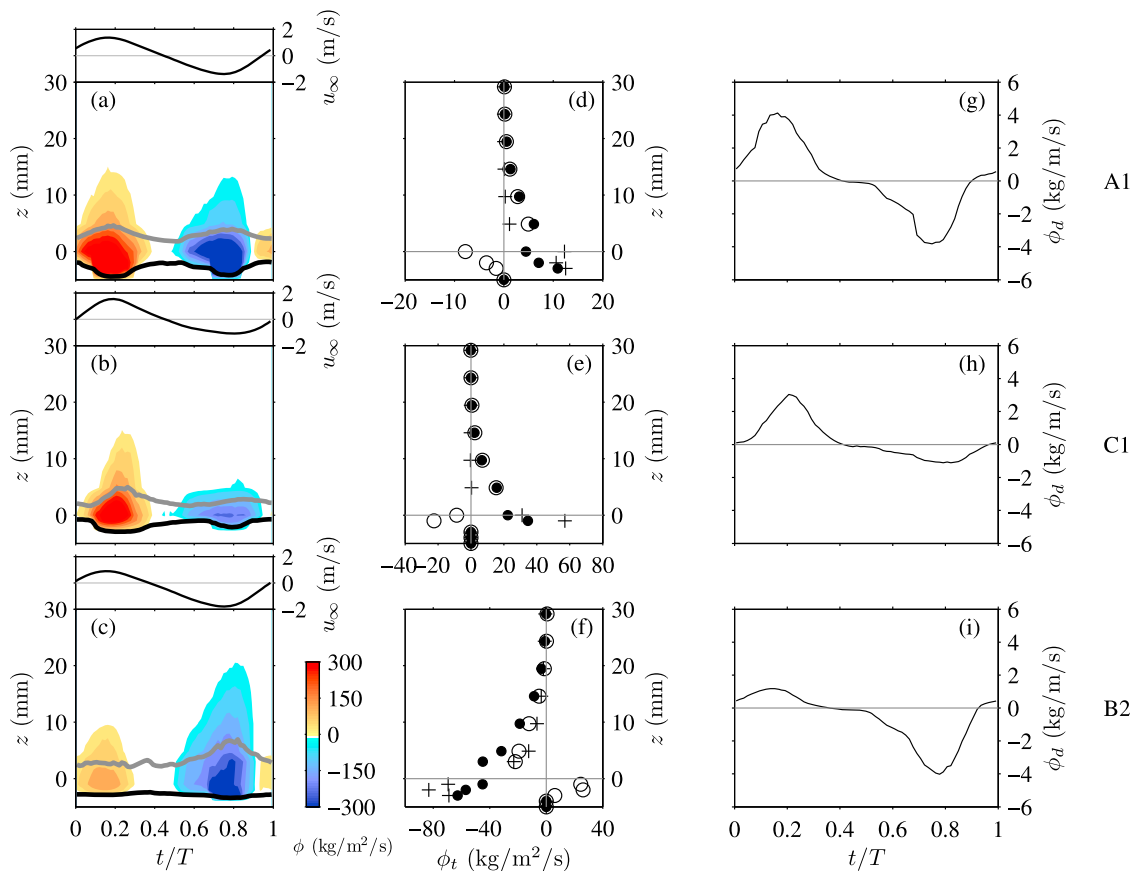
Figure 5. Sand fluxes at (from top to bottom) A1, C1, and B2. (a–c) Time-space diagram of instantaneous flux $\phi(z,t)$. The curved black and gray lines are the instantaneous erosion depth δ_e and the top of the sheet flow layer δ_s, respectively. (d–f) Vertical profiles of oscillatory $\tilde{\phi}_t$ (circles), current-related $\overline{\phi}_t$ (pluses), and net ϕ_t (dots) flux. Note the differences in the scales of the horizontal axes. (g–i) Depth-integrated flux ϕ_d versus nondimensional time t/T.

in velocity asymmetry this likely reflects the reduced duration between $\tilde{u}^-_{\infty,\max}$ and the next flow reversal, allowing less sand to be transported in the negative flow phase. The increase in velocity skewness leads to substantially lower velocities (Figure 1) and concentrations (Figure 3c) in the negative flow phase. For B2 and B4, the increase in velocity asymmetry leads to a larger sand flux in the positive half cycle and hence to a lower negative, net transport rate.

[27] Finally, we computed nondimensional vertical-cumulative sand transport rate distributions, called ogive curves, of $\phi_t (z)$, $\mathrm{Og}_\phi(z)$, to determine the relative importance of the sheet flow and suspension layers to q. Here, $\mathrm{Og}_\phi(z)$ is defined as

$$\mathrm{Og}_\phi(z) = \frac{\int_{z_{\min}}^{z} \phi_t(\hat{z})d\hat{z}}{q}, \qquad (3)$$

where $\hat{z}$ is a dummy integration variable. When, for simplicity, we take $z = 3$ mm as the boundary between the upper sheet flow and suspension layers ($z \approx 3$ mm is the time-averaged value for δ_s in each flow), the sheet flow layer contributes approximately 60%–70% to the net sand transport rate (Figure 6). The majority of this contribution stems from the pick-up layer. Thus, the majority of the flux in velocity-asymmetric flow is concentrated in the sheet-flow

layer, as observed previously in U-tube experiments with sinusoidal flow plus current and velocity-skewed flows [e.g., *Ribberink and Al-Salem*, 1995; *McLean et al.*, 2001].

4. Discussion

4.1. Accuracy

[28] The sheet flow layer is a daunting place to obtain velocity and concentration estimates. Figure 7 compares the flux-based net sand transport rates q to the rates based on the mass conservation method q_{mc} (section 2.3). As can be seen, both rate estimates agree quite well for A1, A3, and C1, even though the net transport from the integration of the fluxes is a small difference between the two large numbers. Small errors in $u(z,t)$, $c(z,t)$, and, hence, q^+ and q^- could have resulted in major differences between the two rate estimates, as for instance observed by *Van der A et al.* [2009]. For B2 and B4, agreement is less good; the flux-based net rates are about 100% and 60% larger for B2 and B4, respectively, than the estimates using the mass-conservation technique. High sand concentrations and the 3 mm vertical bin size of the ADVP prevented a detailed study of the horizontal flow in the pick-up layer. Where possible, we used the ADVP information at $z = -3$ mm to estimate q. This contrasts with the assumption of a linear
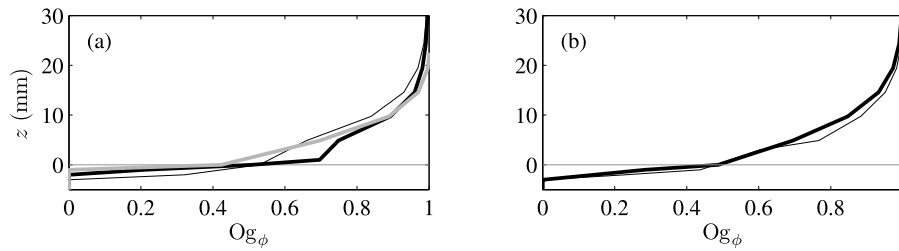
Figure 6. Ogive curves $Og_\phi(z)$ of the time-integrated flux $\phi_t(z)$ for (a) A1 (solid line), A3 (thick solid line), and C1 (thick gray line) and for (b) B2 (solid line) and B4 (thick solid line). The horizontal line is the no-flow bed level, $z = 0$, the approximate boundary between the pick-up and upper sheet flow layers.

velocity profile between the instantaneous erosion depth and $z = 0$, as made in the flux computations of *O'Donoghue and Wright* [2004b] and *Van der A et al.* [2009]. Figure 7 illustrates that the latter approach would have resulted in smaller net transport rates for B2 and B4, bringing them closer to the estimates based on the mass-conservation technique. For A1, A3 and C1 both approaches yield identical results, as the instantaneous erosion depth barely reached below $z = -3$ mm.

[29] Considerable uncertainty ($\approx 1–2$ mm) exists for the precise elevation of the CCM. This uncertainty is caused by uncertainties in the positioning of the CCM with respect to the no-flow bed. This was caused by the slow decline in bed level during each test and by the occasional lack in cross-tube uniformity in bed level. Because vertical gradients in concentration are large in the pick-up layer, even a tiny error in the elevation of the CCM will cause the concentration estimate for a given z to deviate considerably from its "true" value. The z uncertainty of the CCM probes as well as the 1–1.5 mm height of their sampling volume [*Dohmen-Janssen and Hanes*, 2002] also impose considerable uncertainty on the instantaneous erosion depth compared to the thickness of the pick-up layer. Although the temporal evolution of the erosion depth is likely to be accurate, an error in δ_e of 1–2 mm will profoundly affect the net sand transport rate because of the very high concentrations in the pick-up layer. To quantify the inaccuracy in the measured erosion depth, we also estimated the instantaneous erosion depth from integrating all of the concentration measurements above δ_e [*Malarkey et al.*, 2009]

$$\delta_{eE}(t) = -\frac{1}{c_0} \int_{\delta_e(t)}^{\infty} c(t)dz. \qquad (4)$$

The degree of agreement between δ_e and δ_{eE} is a measure of consistency between the erosion depth inferred as the c_0 contour and the erosion depth inferred from the amount of sand in the water column (i.e., above $z = \delta_e$). *Malarkey et al.* [2009] considered δ_e and δ_{eE} to be consistent if they differed by less than 1 mm. It can be seen in Figure 8 that, based on this test, the data for B2 and B4 are consistent; however, for A1, A3, and C1, $\delta_{eE}(t)$ is persistently 1–2 mm larger than $\delta_e(t)$. Thus, there is apparently more sand in the water column than the values of δ_e imply. Whether this means that the δ_e time series are biased low or the source of error stems from the concentration data in the sheet flow and suspension layer (or both) cannot be said from this test. The 1–2 mm difference between δ_e and δ_{eE} is similar to the estimated

uncertainty in the positioning of the CCM probes. The issue of consistency is not meant to criticize the data; instead, it serves as an illustration of their accuracy.

4.2. Relevance to Field Conditions

[30] Although the experiments were conducted at full scale, they do not fully represent the flow conditions at the seabed under real waves. The rigid upper lid of a U-tube implies that vertical orbital motions, wave-induced boundary layer streaming, undertow, and breaking-induced turbulence are not reproduced. Bottom friction acting on real waves causes the horizontal $\tilde{u}$ and vertical $\tilde{w}$ oscillatory motion to be slightly in phase; the resulting nonnegative $\langle \tilde{u}\tilde{w} \rangle$ causes a positive near-bed boundary streaming [*Longuet-Higgins*, 1953]. The absence of the latter type of boundary layer streaming is likely to affect sand transport rates mostly for conditions representative of the shoaling zone with waves dominated by velocity skewness over fine sands (say, $d_{50} < 200~\mu$m). Under these conditions, phase-lag effects contribute to reverse the transport rate from positive to negative [e.g., *Hassan and Ribberink*, 2005; *Ruessink et al.*, 2009]. Under natural waves the increased positive transport rate by the residual flow could change the sign of the net sand transport rate [*Schretlen et al.*, 2009]. For coarser
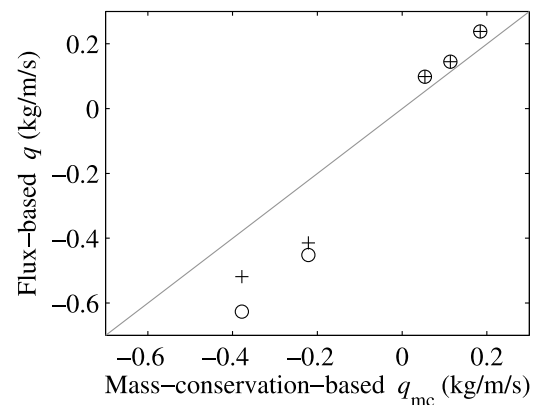
Figure 7. Flux-based net sand transport rates q (i.e., $q^+ + q^-$) versus the net rates based on mass conservation q_{mc} (section 2.3). The circles include the ADVP velocity estimates at $z = -3$ mm in the q computation, while the pluses represent values based on a linear velocity profile between $z = 0$ and the instantaneous erosion depth. The symbols from left to right represent flow conditions B2, B4, A1, A3, and C1.
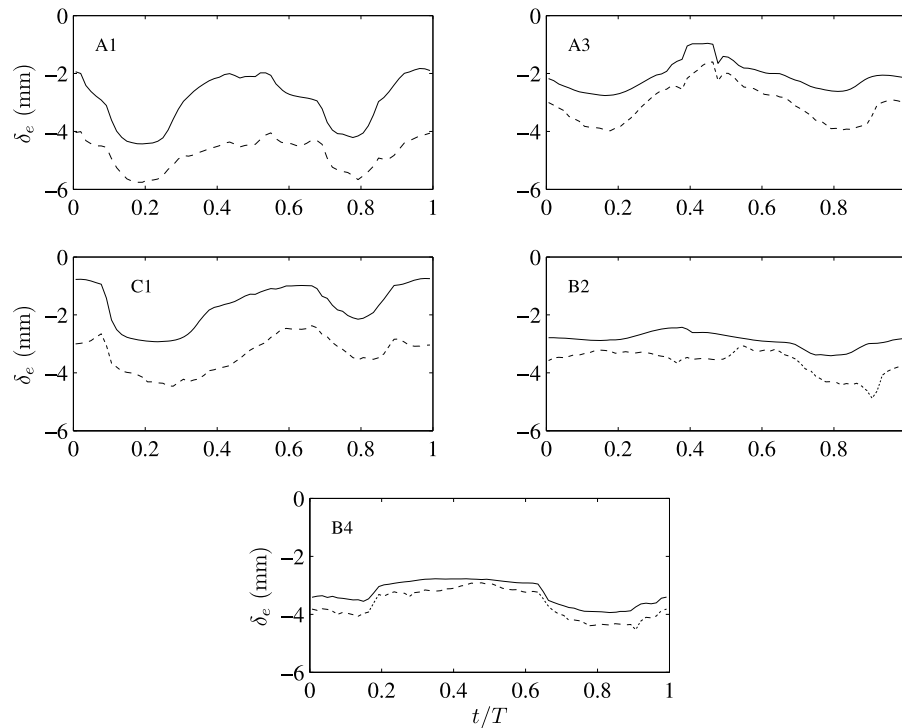
Figure 8. Erosion depth δ_e (solid line) determined as the c_0 contour and erosion depth δ_{eE} (dashed line) quantified from the concentration measurements above δ_e versus nondimensional time t/T for all five flows.

sand, the residual flow-induced flux is of minor importance compared to the onshore-directed oscillatory flux (phase-lag effects are now minimal). *Dohmen-Janssen and Hanes* [2002] and *Schretlen et al.* [2009] indicate that net transport rates under natural velocity-skewed waves may be several times larger than the transport rates under comparable U-tube conditions. In shallower water the mean flow inside the wave bottom boundary layer beneath natural waves is dominated by the compensation for the onshore (Stokes) drift above the wave troughs and is thus negative [e.g., *Reniers et al.*, 2004; *Lentz et al.*, 2008]. In the present experiments we mimicked this undertow by a negative u_t in experiments B2 and B4.

[31] In nature, waves dominated by velocity-asymmetry are typically found in the mid to inner surf zone. Part of the breaking-wave induced turbulence present in the surface roller (the white aerated mass of water on the breaking-wavefront) will penetrate into the water column as coherent vortices [*Nadaoka et al.*, 1989]. Although these vortices disintegrate as they propagate downward, some of the vortices may reach the seabed [*Cox and Kobayashi*, 2000] and stir sand [e.g., *Nadaoka et al.*, 1988; *Scott et al.*, 2009]. How this second source of turbulence affects net sand transport rates is unclear. As pointed out by *Scott et al.* [2009], its effect will depend on the timing of the sand stirring and the near-bed orbital motion. Laboratory [*Cox and Kobayashi*, 2000; *Scott et al.*, 2009] and field observations [*Ruessink*, 2010] indicate breaking-induced turbulence to be strongly intermittent in time, contrasting markedly with the periodic bed-generated turbulence observed here (Figure 1). When breaking-induced turbulence is the dominant source of the pick-up of sand from the bed, its intermittent character will

cause sand suspension to be unrelated to the wave phase and, thus, the oscillatory transport rate to reduce to 0. On the other hand, the additional turbulence will bring more sand into suspension (and to greater distances above the bed as well), causing the current-related transport rate to increase. Measurements of turbulence fluctuations, oscillatory and mean-flow velocities, and sand concentrations beneath breaking waves are needed to establish better understanding of breaking-wave effects on sand transport rates.

5. Conclusions

[32] Using instantaneous (10 Hz) vertical profiles of horizontal velocity and sand concentration from the suspension layer to within the pick-up layer in a $d_{50} = 200~\mu$m sand, we have demonstrated that the net positive transport rate beneath regular velocity-asymmetric oscillatory flow results from large, but opposing instantaneous sand fluxes during the positive and negative flow phase. With an increase in velocity asymmetry and, in particular, velocity skewness, the imbalance between the positive and negative sand fluxes increases. This causes an increase in the net sand transport rate, a trend that is consistent with the observed increase in skewness of the oscillatory bed shear stress. The thicker sheet flow layer during the negative-to-positive flow reversal for more velocity-asymmetric flow illustrates that an increasing amount of sand stirred during the negative flow phase has not settled by the time of this flow reversal and is subsequently transported during the positive flow phase. Compared to earlier experiments with finer sands, the importance of these phase lag effects to the net transport rate in velocity-asymmetric flow is minor. In the vertical, the

oscillatory fluxes above the no-flow bed are positive and dominate over the fluxes induced by the residual flow. Within the pick-up layer the oscillatory fluxes are negative, while the fluxes induced by the residual flow are now positive and no longer negligible. The effect of a 0.4 m/s opposing current is to cause more sand stirring during the negative than the positive flow phase and, hence, to result in negative oscillatory fluxes above the no-flow bed. These oscillatory fluxes and the current-related fluxes are of comparable magnitude. We find no evidence that plug flow was of importance to the sand transport in our experiments.

References

Abreu, T., M. J. Franca, P. A. Silva, and F. Sancho (2009), Estimation of sediment particle velocities in the sheet flow: Cross-correlation and wavelet analysis, in *Proceedings of River, Coastal and Estuarine Morphodynamics*, pp. 1051–1056, Taylor and Francis, London.

Abreu, T., P. A. Silva, F. Sancho, and A. Temperville (2010), Analytical approximate wave form for asymmetric waves, *Coastal Eng.*, 57, 656–667.

Betteridge, K. F. E., P. D. Thorne, and R. D. Cooke (2008), Calibrating multi-frequency acoustic backscatter systems for studying near-bed suspended sediment transport processes, *Cont. Shelf Res.*, 28, 227–235.

Bosman, J. J., E. T. J. M. van der Velden, and C. H. Hulsbergen (1987), Sediment concentration measurement by transverse suction, *Coastal Eng.*, 11, 353–370.

Calantoni, J., and J. A. Puleo (2006), Role of pressure gradients in sheet flow of coarse sediments under sawtooth waves, *J. Geophys. Res.*, 111, C01010, doi:10.1029/2005JC002875.

Cox, D. T., and N. Kobayashi (2000), Identification of intense, intermittent coherent motions under shoaling and breaking waves, *J. Geophys. Res.*, 105, 14,223–14,236.

Davies, A. G., and Z. Li (1997), Modelling sediment transport beneath regular symmetrical and asymmetrical waves above a plane bed, *Cont. Shelf Res.*, 17, 555–582.

Dibajnia, M., and A. Watanabe (1998), Transport rate under irregular sheet flow conditions, *Coastal Eng.*, 35, 167–183.

Dick, J., and J. Sleath (1992), Sediment transport in oscillatory sheet flow, *J. Geophys. Res.*, 97, 5745–5758.

Doering, J. C., and A. J. Bowen (1995), Parameterization of orbital velocity asymmetries of shoaling and breaking waves using bispectral analysis, *Coastal Eng.*, 26, 15–33.

Dohmen-Janssen, C. M., and D. M. Hanes (2002), Sheet flow dynamics under monochromatic non-breaking waves, *J. Geophys. Res.*, 107(C10), 3149, doi:10.1029/2001JC001045.

Dohmen-Janssen, C. M., D. F. Kroekenstoel, W. N. Hassan, and J. S. Ribberink (2002), Phase lags in oscillatory sheet flow: Experiments and bed load modelling, *Coastal Eng.*, 46, 61–87.

Dong, P., and K. Zhang (2002), Intense near-bed sediment motions in waves and currents, *Coastal Eng.*, 45, 75–87.

Drake, T. G., and J. Calantoni (2001), Discrete particle model for sheet flow sediment transport in the nearshore, *J. Geophys. Res.*, 106, 19,859–19,868.

Elfrink, B., D. M. Hanes, and B. G. Ruessink (2006), Parameterization and simulation of near bed orbital velocities under irregular waves in shallow water, *Coastal Eng.*, 53, 915–927.

Elgar, S., and R. T. Guza (1985), Observations of bispectra of shoaling surface gravity waves, *J. Fluid Mech.*, 161, 425–448.

Foster, D. L., A. J. Bowen, R. A. Holman, and P. Natoo (2006), Field evidence of pressure gradient induced incipient motion, *J. Geophys. Res.*, 111, C05004, doi:10.1029/2004JC002863.

Gonzalez-Rodriguez, D., and O. S. Madsen (2007), Seabed shear stress and bedload transport due to asymmetric and skewed waves, *Coastal Eng.*, 54, 914–929.

Hassan, W. N., and J. S. Ribberink (2005), Transport processes of uniform and mixed sands in oscillatory sheet flow, *Coastal Eng.*, 52, 745–770.

Hsu, T. J., and D. M. Hanes (2004), Effects of wave shape on sheet flow sediment transport, *J. Geophys. Res.*, 109, C05025, doi:10.1029/2003JC002075.

Hurther, D., and U. Lemmin (2001), A correction method for turbulence measurements with a 3D acoustic Doppler velocity profiler, *J. Atmos. Ocean. Technol.*, 18, 446–458.

King, D. B. (1991), Studies in oscillatory flow bedload sediment transport, Ph.D. thesis, Univ. of Calif., San Diego.

Lentz, S. J., M. Fewings, P. Howd, J. Fredericks, and K. Hathaway (2008), Observations and a model of undertow over the inner continental shelf, *J. Phys. Oceanogr.*, 38, 2341–2357.

Longuet-Higgins, M. S. (1953), Mass transport in water waves, *Philos. Trans. R. Soc. London A*, 245, 535–581.

Malarkey, J., S. Pan, M. Li, T. O'Donoghue, A. G. Davies, and B. A. O'Conner (2009), Modelling and observation of oscillatory sheet-flow sediment transport, *Ocean Eng.*, 36, 873–890.

McLean, S. R., J. S. Ribberink, C. M. Dohmen-Janssen, and W. N. Hassan (2001), Sand transport in oscillatory sheet flow with mean current, *J. Waterway Port Coastal Ocean Eng.*, 127(3), 141–151.

Nadaoka, K., S. Ueno, and T. Igarashi (1988), Sediment suspension due to large scale eddies in the surf zone, in *Proceedings of the 21st International Conference on Coastal Engineering*, pp. 1646–1660, ASCE, New York.

Nadaoka, K., M. Hino, and Y. Koyano (1989), Structure of the turbulent flow field under breaking waves in the surf zone, *J. Fluid Mech.*, 204, 359–387.

Nielsen, P. (1992), *Coastal Bottom Boundary Layers and Sediment Transport*, 324 pp., World Sci., Singapore.

Nielsen, P. (2006), Sheet flow sediment transport under waves with acceleration skewness and boundary layer streaming, *Coastal Eng.*, 53, 749–758.

O'Donoghue, T., and S. Wright (2004a), Concentrations in oscillatory sheet flow for well sorted and graded sands, *Coastal Eng.*, 50, 117–138.

O'Donoghue, T., and S. Wright (2004b), Flow tunnel measurements of velocities and sand flux in oscillatory sheet flow for well-sorted and graded sands, *Coastal Eng.*, 51, 1163–1184.

Reniers, A. J. H. M., E. B. Thornton, T. P. Stanton, and J. A. Roelvink (2004), Vertical flow structure during Sandy Duck: Observations and modeling, *Coastal Eng. 51*, 237–260, doi:10.1016/j.coastaleng.2004.02.001.

Ribberink, J. S., and A. A. Al-Salem (1994), Sediment transport in oscillatory boundary layers in cases of rippled beds and sheet flow, *J. Geophys. Res.*, 99, 12,707–12,727.

Ribberink, J. S., and A. A. Al-Salem (1995), Sheet flow and suspension of sand in oscillatory boundary layers, *Coastal Eng.*, 25, 205–225.

Ribberink, J. S., J. J. van der Werf, T. O'Donoghue, and W. N. M. Hassan (2008), Sand motion induced by oscillatory flows: Sheet flow and vortex ripples, *J. Turbulence*, 9, 1–32.

Roelvink, J. A., and M. J. F. Stive (1989), Bar-generating cross-shore flow mechanisms on a beach, *J. Geophys. Res.*, 94, 4785–4800.

Ruessink, B. G. (2009), Intrawave measurements of suspended sediment concentrations: the TRANSKEW ABS data report, *IMAU Rep. R09-01*, Dept. of Phys. Geogr., Utrecht Univ., Utrecht, Netherlands.

Ruessink, B. G. (2010), Observations of turbulence within a natural surf zone, *J. Phys. Oceanogr.*, 40, 2696–2712.

Ruessink, B. G., T. J. J. van den Berg, and L. C. van Rijn (2009), Modeling sediment transport beneath skewed asymmetric waves above a plane bed, *J. Geophys. Res.*, 114, C11021, doi:10.1029/2009JC005416.

Schretlen, J. L. M., J. S. Ribberink, and T. O'Donoghue (2009), Sand transport under full-scale surface waves, paper 123 in *Proceedings Coastal Dynamics '09*, World Sci., Singapore.

Scott, N. V., T. J. Hsu, and D. Cox (2009), Steep wave, turbulence, and sediment concentration statistics beneath a breaking wave field and their implications for sediment transport, *Cont. Shelf Res.*, 29, 2303–2317.

Silva, P. A., A. Temperville, and F. S. Santos (2006), Sand transport under combined current and wave conditions: A semi-unsteady, practical model, *Coastal Eng.*, 53, 897–913.

Sleath, J. F. A. (1999), Conditions for plug formation in oscillatory flow, *Cont. Shelf Res.*, 19, 1643–1664.

Suntoyo, H. Tanaka, and A. Sana (2008), Characteristics of turbulent boundary layers over a rough bed under saw-tooth waves and its application to sediment transport, *Coastal Eng.*, 55, 1102–1112.

Svendsen, I. A. (1987), Analysis of surf zone turbulence, *J. Geophys. Res.*, 92, 5115–5124.

Thorne, P. D., and D. M. Hanes (2002), A review of acoustic measurement of small-scale sediment processes, *Cont. Shelf Res.*, *22*, 603–632.

Thorne, P. D., and P. J. Hardcastle (1997), Acoustic measurements of suspended sediments in turbulent currents and comparison with in-situ samples, *J. Acoust. Soc. Am.*, *101*, 2603–2614.

Thorne, P. D., G. P. Holdaway, and P. J. Hardcastle (1995), Constraining acoustic backscatter estimates of suspended sediment concentration profiles using the bed echo, *J. Acoust. Soc. Am.*, *98*, 2280–2288.

Van der A, D. A., T. O'Donoghue, A. G. Davies, and J. S. Ribberink (2008), Effects of acceleration skewness on rough bed oscillatory boundary layer flow, in *Proceedings of the 31st International Conference on Coastal Engineering*, pp. 1583–1595, World Sci., Singapore.

Van der A, D. A., T. O'Donoghue, and J. S. Ribberink (2009), Sheet flow sand transport processes in oscillatory flow with acceleration skewness, paper 133 in *Proceedings Coastal Dynamics'09*, World Sci., Singapore.

Van der A, D. A., T. O'Donoghue, and J. S. Ribberink (2010), Measurements of sheet flow transport in acceleration-skewed oscillatory flow and comparison with practical formulations, *Coastal Eng.*, *57*, 331–342.

Watanabe, A., and S. Sato (2004), A sheet-flow transport rate formulations for asymmetric, forward-leaning waves and currents, in *Proceedings of the 29th International Conference on Coastal Engineering*, pp. 1703–1714, ASCE, New York

T. Abreu, Department of Civil Engineering, Polytechnic Institute of Viseu, ESTV, Campus de Repeses, 3504-510 Viseu, Portugal. (tabreu@estv.ipv.pt)

H. Michallet, Laboratoire des Ecoulements Géophysiques et Industriels, CNRS, Université de Grenoble, F-38041 Grenoble, France. (herve.michallet@hmg.inpg.fr)

B. G. Ruessink, Department of Physical Geography, Faculty of Geosciences, Institute for Marine and Atmospheric Research Utrecht, Utrecht University, PO Box 80.115, NL-3508 TC, Utrecht, Netherlands. (g.ruessink@geo.uu.nl)

F. Sancho, LNEC-DHA, National Civil Engineering Laboratory, Lisbon 1700-066, Portugal. (fsancho@lnec.pt)

P. A. Silva, CESAM and Departamento de Fisica da Universidade de Aveiro, Aveiro 3810-193, Portugal. (psilva@ua.pt)

D. A. Van der A, School of Engineering, King's College, University of Aberdeen, Aberdeen AB24 3UE UK. (d.a.vandera@abdn.ac.uk)

J. J. Van der Werf, Morphology and Sedimentary Systems, Deltares, NL-2600 MH Delft, Netherlands. (jebbe.vanderwerf@deltares.nl)